Optical rheology for live cell membranes

By

YongKeun Park
B.S., Seoul National University (2004)

Submitted to the Department of Mechanical Engineering
in Partial Fulfillment of the Requirements for the Degree of
Master of Science in Mechanical Engineering

at the
Massachusetts Institute of Technology

May 2007
[June 2007]

Signature of Author: _____
Department of Mechanical Engineering
May 8, 2005

Certified by: _____
Michael S. Feld
Professor, Department of Physics
Thesis Supervisor

Certified by: _____
Subra Suresh
Professor, Department of Mechanical Engineering
Thesis Co-Supervisor

Accepted by: _____
Lallit Anand
Chairman, Graduate Thesis Committee

Optical rheology for live cell membranes

By

YongKeun Park

Submitted to the Department of Mechanical Engineering on May 21, 2007 in Partial Fulfillment of the Requirements for the Degree of Master of Science in Mechanical Engineering

ABSTRACT

We present a novel optical methodology including both instrumentation and theory aimed at retrieving the full viscoelastic information of cell membrane material properties. Red blood cells (RBC) are chosen for this study because of their simple structure, which consists of a bi-layer cell membrane supported by a cytoskeleton enclosing a homogeneous fluid. The full complex modulus of RBC in terms of temporal frequency and spatial frequency is retrieved without contact, for the first time to our knowledge. Sub-nanometer sensitivity diffraction phase and fluorescence microscopy (DPF) quantifies non-invasively three dimensional morphological information of live cell with high speed. The fluctuation dissipation theory and generalized Stokes-Einstein relationship provide the complex modulus associated with the cell membrane, in a spatially-resolved manner. This information is used to retrieve the dynamic and spatial behavior of red blood cell membranes during the process of shape deterioration. The viscoelasticity results on RBC strongly correlate with cell morphology. Thus, we find that the cell evolution from a normal, doughnut shape to a spheroid can be interpreted from a viscoelastic point of view as a liquid-solid transition.

Thesis supervisor: Michael S. Feld, Ph.D.

Title: Professor, Department of Physics
Director, George Harrison Spectroscopy Laboratory

Thesis co-supervisor: Subra Suresh, Sc.D.

Title: Professor of Materials Science and Engineering
Professor of Biological Engineering
Professor of Mechanical Engineering

ACKNOWLEDGEMENT

The author sincerely thanks his research advisor Prof. Michael S. Feld for his personal attention and support as well as scientific guidance. He gave the author uncountable opportunities. The author also thanks to co-advisor Prof. Subra Suresh for the discussion and guidance in the research.

The author thanks to all members of George R. Harrison Spectroscopy Laboratory. Special thanks to Dr. Gabriel Popescu for his advising on the research projects and being a mentor, and LCI members for friendship.

Additional thanks to Dr. Euiheon Chung for his support.

Special thanks to my wife, Saeeun Choi for her love.

TABLE OF CONTENTS

Chapter 1. Introduction

1.1 Live Cell Imaging

Since Antoine van Leeuwenhoek used his home-built microscope for cell observation, optical microscopy has been used for more than 300 years in the field of biology and medicine [1]. One of the reasons why optical microscopic techniques are broadly used is an intrinsic characteristic of light – it is non-invasive and non-harmful to living cells. The transparency of cells and small organisms, however, made cell imaging difficult because the conventional microscope, which is based on the intensity of optical wave, does not provide enough contrast enough for a transparent sample. Phase Contrast Microscopy, invented by Frits Zernike, solved this problem by converting optical phase information into the intensity, image and made it easy for biologists to access and study many biological phenomena related to living cells [2]. Even thought phase contrast microscopy is very commonly used to provide contrast of transparent live cell, it is qualitative and does not provide quantitative information about the refractive index and cell thickness.

For the past few decades, many quantitative imaging techniques have been developed for cell imaging, such as Scanning Electronic Microscopy (SEM) [3] and Atomic Force Microscopy (AFM) [4]. SEM is an electron microscopy technique which produces images by detecting electrons which are emitted from the sample surface due to excitation by the primary electron beam. SEM offers higher resolving power than optical microscopy but it requires silver or platinum coating of the samples prior to imaging, which is not compatible with live cell imaging. AFM is a scanning image technique with sub-nanometer resolution. When a micro-scale cantilever with a sharp tip (probe) scans the sample point by point, the laser reflected from the cantilever gives information about the height of the sample. The AFM techniques can be used on live cells, but slow point scanning limits various biological applications. Even though conventional quantitative imaging techniques such as SEM and AFM provide high lateral resolution, they are not well-suited for live cell imaging.

1.2 Quantitative Phase Microscopy

Over the past decade, the development of quantitative phase imaging techniques to access information about morphology and dynamics of living cells has received increased scientific interest [5-10]. Quantitative phase microscopy utilizes phase delay of the light to retrieve quantitative information of the cell. When a plane wave of light passes through a transparent cell, it undergoes phase delay, i.e. an optical path length change which can be expressed as the combination of the refractive index difference and the thickness of the cell. If one can retrieve this phase delay quantitatively, it is possible to reconstruct the morphology of the cell on the nanometer scales. Quantitative phase microscopic techniques can be divided on how the optical phase information is modulated: spatial modulation, temporal modulation, and polarization modulation.

Fourier Phase Microscopy is a common-path interferometric imaging technique which combines the principles of phase contrast microscopy and phase shifting interferometry, such that

the scattered and unscattered light from a sample are used as the object and reference fields of an interferometer [5]. Hilbert Phase Microscopy measures quantitative phase images from only one spatial interferogram recording [6]. The phase information is modulated on the sample arm. The reference arm, with uniform phase distribution, is brought into interference with the sample arm at a particular angle, which generates spatial fringe patterns. As only one interferogram is required for phase imaging, the speed of HPM is only limited by the frame rate of the recording camera. However differential phase noise (from air drifting or fluctuations, etc) deteriorates the stability of HPM. Active noise control using a feed-back loop can be combined to achieve high sensitivity [32]. Diffraction Phase Microscopy has a common path geometry which is achieved by using a diffraction grating as a beam splitter [7]. The grating generates many diffraction orders and two of these are used as signal and reference arms of a compact Mach-Zehnder interferometer. Since these two arms are passing almost through the same optical path, most of the phase noise is mutually cancelled, thus providing high stability without any electrical noise control equipment. Digital holographic microscopy (DHM) is another spatial modulation method [8]. It is similar to HPM in terms of the interferometer geometry. DHM acquires the digital hologram at off-focus planes and digitally focuses the image. Heterodyne Mach-Zehnder Phase Microscopy modulates the phase delay of the sample via temporal modulation of the light beam [9]. It utilizes Mach-Zender inteferometry and an acousto-optic modulator (AOM) change the temporal frequency of one of the arms. Polarization was also used for retrieving quantitative phase images in a quadrature arrangement. [10]

1.3 Cell membrane dynamics

Cells produce and react to forces actively and selectively through their mechanical framework, the cytoskeleton. In order to study the dynamic and functional roles of the cytoskeleton within the cell, it is critical to understand its material properties. Over the past decade a number of different techniques have been used to study the microrheology of live cells [11]. Among them, pipette aspiration [12], electric field deformation [13], and optical tweezers [14] provide quantitative information about the shear and bending moduli of RBC membranes under static conditions. Figure 1 illustrates how these types of techniques work [11]. Atomic force microscopy (AFM) (Fig.1A) and magnetic twisting cytometry (Fig.1B) are methods that can probe cell components at a force resolution of 10^{-10} and 10^{-12} N, respectively, and a displacement resolution of at least 1 nm micropipette aspiration (Fig.1C) and optical trapping (Fig.1D) can deform an entire cell at a force resolution of 10^{-10} and 10^{-11} N, respectively. Shear flow (Fig.1E) and substrate stretching (Fig.1F) methods are capable of evaluating the mechanical response of a population of cells.

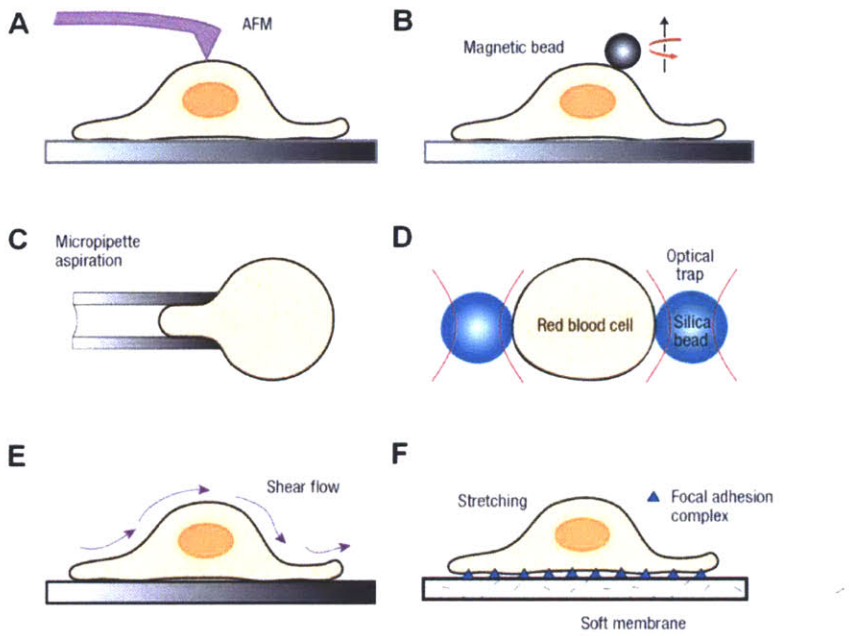

Figure 1. Schematic representation of experimental technique used to probe living cells (reproduced from [11]).

However, dynamic, frequency-dependent knowledge of the RBC mechanical response is very limited [15]. RBC thermal fluctuations (flickering) have been studied for more than a century to better understand the interaction between the lipid bilayer and the cytoskeleton [16-19]. Nevertheless, quantifying these motions is experimentally challenging, as they develop at the nanometer and millisecond scales across the entire cell, and, thus, reliable spatial and temporal data are currently not available.

This thesis presents novel instrumentation and theoretical modeling to retrieve the frequency dependent complex modulus of the RBC membrane. RBCs are chosen for this study because of their simple structure, which consists of a bi-layer cell membrane supported by a cytoskeleton enclosing a homogeneous fluid. Diffraction phase microscopy (DPM) provides dynamic quantitative phase information with high frame rate and high stability, which can be interpreted as the three dimensional morphological information of a sample with the sub nanometer stability. We also develop the generalized fluctuation dissipation theory to calculate dynamics viscoelasiticy of cell membranes based on the information of dynamic fluctuations measured with diffraction phase microscopy. This non-contact optical technique can be used to study the viscoelastic properties of thin membranes in general, as well as biological samples such as red blood cells (RBC). This method does not require any sample preparation, thus makes it possible to measure samples with high sensitivity and throughput. The viscoelasticity results from RBC strongly correlate with cell morphology. Thus, we show that cell evolution from a normal, doughnut shape to a spheroid can be interpreted from a viscoelastic point of view as a liquid-glass transition.

Chapter 2. Instrumentation

2.1 Diffraction Phase Microscopy

Here we use diffraction phase microscopy (DPM), a novel, highly sensitive, optical imaging technique, to quantify the flickering of RBC membranes and extract the frequency-dependent viscosity and elasticity moduli of RBCs. DPM provides quantitative maps of the optical paths across the living cells with unprecedented stability [20, 21]. This optical path-length information can be readily translated into cell thickness, as the RBCs are optically homogeneous, i.e. characterized by a constant refractive index.

The DPF experimental setup is depicted in Fig. 2 and Fig. 3. An inverted microscope (IX71, Olympus Inc.) is utilized for the sample stage. An Ar^{2+} laser (λ=514μm) is used as an illumination source for transmission phase imaging. Through its video output port, the microscope produces the image of the sample at the image plane IP1 with magnification M=40. The lens system L1-L2 is used to collimate the un-scattered field (spatial DC component) and further magnify the image by a factor f2/ f1=3, at the plane IP2. An amplitude grating G is placed at IP2, which generates multiple diffraction orders containing full spatial information about the sample image. The goal is to isolate the 0^{th} and 1^{st} orders and to create a common-path Mach-Zender interferometer, with the 0th order as the reference beam and the 1st order as the sample beam. To accomplish this, a standard 4-f spatial filtering lens system L3-L4 is used. This system selects only the 0^{th} and 1^{st} order and generates the final interferogram at the CCD plane. The 0^{th} order beam is low-pass filtered using a pinhole placed at the Fourier plane L3 so that it becomes a plane wave after passing through lens L4. The spatial filter allows passing the entire frequency information of the 1^{st} order beam and blocks the high frequency information of the 0^{th} order beam. Compared to conventional Mach-Zender interferometers, the two beams propagate through the same optical component, which significantly reduces the longitudinal phase noise without the need for active stabilization. A CCD camera (Photomax X360, Princeton instrument) is used to capture the interferogram. The CCD has a resolution of 512x512 pixels, and each pixel is 16x16 μm in size. From the interferogram recorded, the quantitative phase image is extracted via a spatial Hilbert transform which is explained in the detail in the following section. The grating period is 30 μm, which is smaller than the diffraction spot of the microscope at the grating plane (47 μm). Thus, the optical resolution of the microscope is preserved.

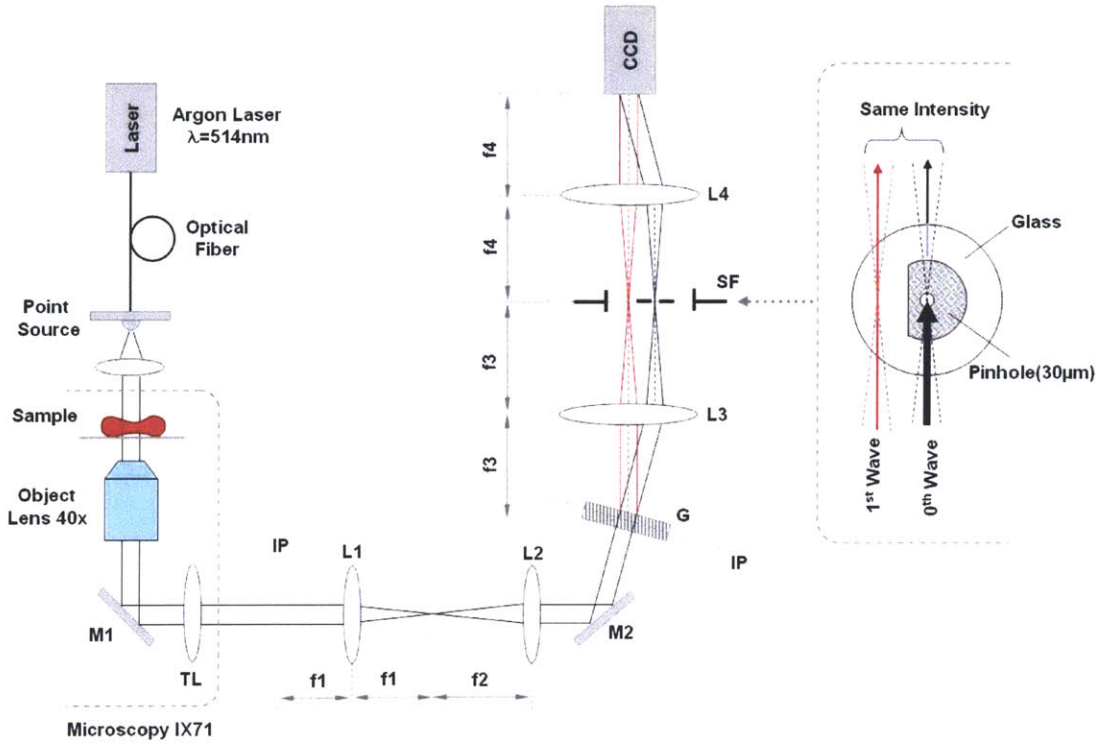

Figure 2. DPM setup. $M_{1,2}$, mirrors; $L_{1\sim4}$ lenses ($f_{1\sim4}$, respective focal lengths); G, grating; SF, spatial filter; IP, image plane.

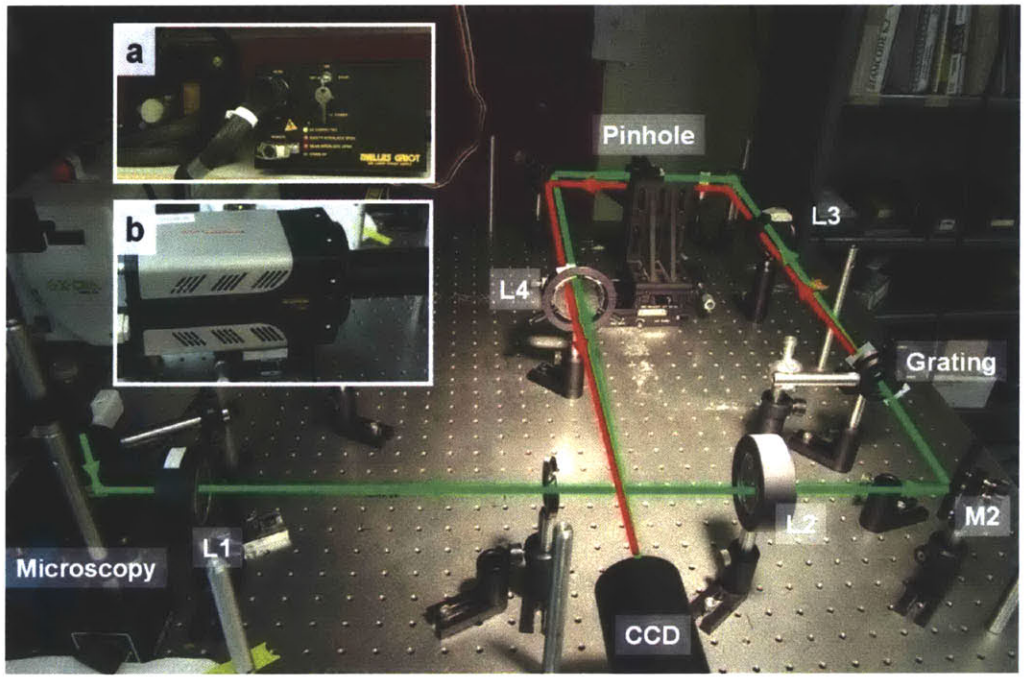

Figure 3. Picture of the setup. A. Argon ion laser; B. CCD camera. $M_{1,2}$, mirrors; $L_{1\sim4}$ lenses.

The biological sample is located on the microscope stage, and as the plane wave beam transverses the sample the optical phase is delayed depending on the refractive index and the thickness of the sample. Through its video output port, the microscope produces the image of the sample at the image plane with magnification M=40, which is from the objective lens of the microscope. Note that the field at the image plane is

$$E_1 = A(x,y)e^{j\phi(x,y)}, \tag{1}$$

where $A(x,y)$ is the amplitude, which has the information about the absorption of the sample, and $\phi(x,y)$ is the phase information of interest.

An amplitude grating G is placed at the image plane, which generates multiple diffraction orders containing full phase information about the sample image. The goal is to isolate the 0^{th} and 1^{st} orders and to create a common-path Mach-Zender interferometer, with the 1^{st} diffraction order as the reference beam and the 0^{th} diffraction order as the sample beam. To achieve this, a standard 4-F spatial filtering lens system L1-L2 is used. This system selects only the 0^{th} and 1^{st} order, and the other beams are blocked. Thus the field after the grating is

$$E_2 = \frac{1}{2}A(x,y)e^{j\phi(x,y)} + \frac{1}{\pi}A(x,y)e^{j\phi(x,y)}e^{-j2\pi f_0 x}, \tag{2}$$

where $f_0 = \dfrac{1}{\Lambda_G}$ is the spatial frequency of the 1^{st} order beam and Λ_G is fringe size of the grating. The 1^{st} order beam is low-pass filtered using a pinhole placed at the Fourier plane so that it becomes a plane wave after passing through lens L2. The spatial filter allows passing the entire frequency information of the 1^{st} order beam and blocks the high frequency information of the 0^{th} beam. Note that, as a consequence of the central ordinate theorem, the reference field is proportional to the spatial average of the microscope image field,

$$E_R = \frac{1}{\pi}\bar{A}e^{j\bar{\phi}}e^{-j2\pi f_0 x} = \frac{1}{S}\iint A(x,y)e^{j\phi(x,y)}dS \cdot e^{-j2\pi f_0 x}, \tag{3}$$

where S is the total image area. At the CCD plane both sample and reference beams interfere so that interferometric fringe patterns are recorded, and the intensity pattern is

$$I = \left|E_S + E_R\right| = \frac{1}{2}A(x,y)e^{j\phi(x,y)} + \frac{1}{\pi}\bar{A}e^{j\bar{\phi}}e^{-j2\pi f_0 x}. \tag{4}$$

Compared to conventional Mach-Zender interferometers, the two beams propagate through the same optical component, which significantly reduces the longitudinal phase noise significantly.

2.2 Numerical retrieval of quantitative phase

The diffraction phase microscopy utilizes numerical analysis powered by computer image processing. Fig. 4 illustrates the numerical procedure.

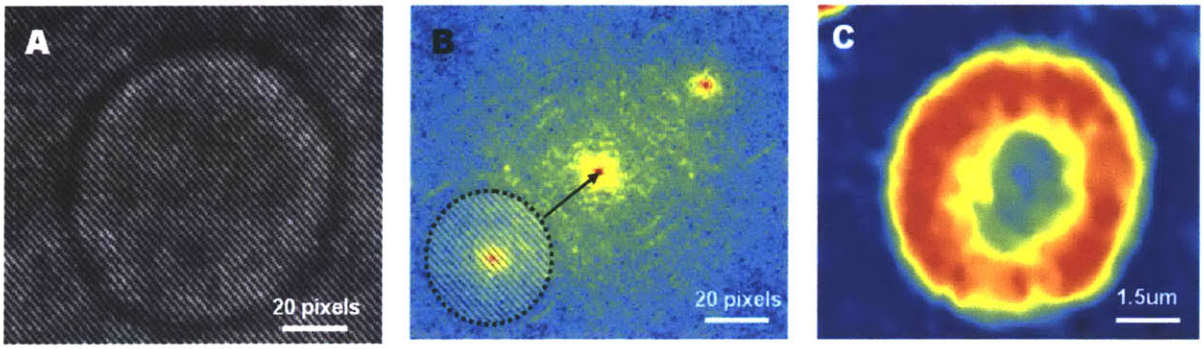

Figure 4. Numerical image processing procedure: A. interferometric fringe pattern, B. 2D FFT image of A, and C. quantitative phase map corresponding fig 4.A

Fig 4A shows the interferometric fringe pattern which is recorded on the CDD plane. Generally, as long as only linear spatial frequencies are recorded, the holographic fringe pattern can be expressed as

$$\begin{aligned} I &= a(x,y) + b(x,y)\cos\{2\pi f_x x + \phi(x,y)\} \\ &= a(x,y) + c(x,y)e^{j2\pi f_0 x} + c^*(x,y)e^{-j2\pi f_0 x} \\ c(x,y) &= \frac{1}{2}b(x,y)e^{j\phi(x,y)}, \end{aligned} \tag{5}$$

where $f_0 = \frac{1}{\Lambda}$, with Λ the fringe spacing. As 4-F optical filtering system is used, only the horizontal spatial frequency term is considered here this is not clear. The relationship between Λ, the fringe spacing of the interferometric fringe pattern and Λ_G, the fringe spacing of the grating G is

$$\Lambda = \frac{f_2}{f_1}\Lambda_G, \tag{6}$$

Two dimensional Fast Fourier Transform (2D FFT) of the interferometric fringe pattern is then implemented as in Figure 4B and it can be expressed as

$$\Im(I) = A(f_x, f_y) + C(f_x - f_0, f_y) + C^*(f_x + f_0, f_y) \tag{7}$$

Now, if we then take the 1st order area only out of the $\Im(I)$ and shift it to the center as illustrated on the Fig4 B as the dotted red circle, the spatial frequency field is modified as

$$\Im^* = C(f_x, f_y), \tag{8}$$

and another 2D FFT on this $\Im^*$ gives the result of the inverse Fourier Transform as

$$\Im^{-1}(\Im(I^*)) = I^* = c(x,y) = \frac{1}{2}b(x,y)e^{j\phi(x,y)} \tag{9}$$

You need the connection to complex analytic signals. Taking the logarithm will divide (x) into real and imaginary parts.

$$\log(c) = \log\left(\frac{1}{2}b(x,y)\right) + i\phi(x,y) \tag{10}$$

Finally we obtain the quantitative phase information by taking imaginary part of this equation.

2.3 Fluorescence and Diffraction phase Microscopy

Quantitative phase imaging has the remarkable ability of providing detailed information about complex phenomena such as cell motility, dry mass growth, and membrane fluctuations without sample preparation. However, this type of measurement lacks specificity, i.e. the optical path-length detected is not characteristic of a certain molecular structure.

In order to measure simultaneously quantitative phase and fluorescence images from cellular structures, diffraction phase microscopy can be combined with fluorescence module which may be called as diffraction phase and fluorescence microscopy (DPF) [22]. This type of investigation combines for the first time optical path-length maps of live cells with images of specific structures tagged by fluorophores.

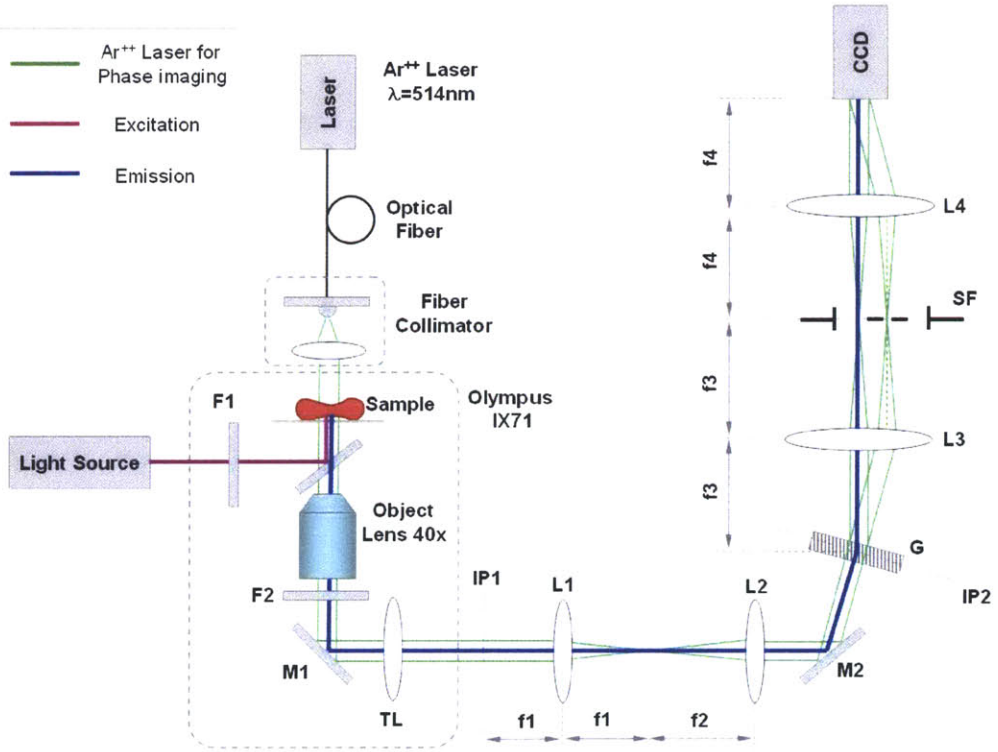

Figure 5. DPF setup. F1,2, filters; M1,2, mirrors; L1-4 lenses (f1-4, respective focal lengths); G, grating; SF, spatial filter; IP1,2, image planes; SF, spatial filter.

The DPF experimental setup is depicted in Fig. 5. Over all, the setup is based on DPM except for the fluorescent module. An inverted microscope (IX71, Olympus Inc.) is equipped for standard epi-fluorescence using a UV lamp and an excitation-emission filter pair, F1-F2. For the purpose of phase imaging purpose, the optical path is identical to that of diffraction phase microscopy. For fluorescence imaging, the sample is excited by epi-fluorescence UV lamp and emits fluorescence light along the same path as for phase imaging. After the grating, the fluorescence emission passing though the 1st diffraction order is imaged by the same camera and

the 0^{th} order of fluorescence can be neglected because the fluorescent light is spatially incoherent , and thus generates a much larger spot than the pinhole, which blocks the 0^{th} order almost entirely.

In order to illustrate the combined phase-fluorescence imaging capability, we performed experiments of kidney (mesangial) cells in culture. The cells were imaged directly in culture dishes surrounded by a culture medium. Prior to imaging, the cells were treated with Hoest solution for 60 minutes at 38°C and 5% CO_2. This fluorescent dye binds to the DNA molecules and is commonly used to reveal the cell nuclei. Figure 3 shows an example of our composite investigation. The quantitative phase image of a single cell is shown in Fig. 6(a). Figure 6(b) shows the fluorescence image of the same cell, where it becomes apparent that the cell is in the processes of mitosis, as indicated by the two separated nuclei. Figure 6(c) shows the composite image. By taking advantage of the difference in the spatial coherence of the two fields, the fluorescence and phase imaging light pass through the same optics, without the need for separation by using, for instance, dichroic mirrors. While the diffraction grating provides a stable geometry for interferometry, it introduces light losses which may affect fluorescence imaging especially of weak fluorophores. However, this aspect can be ameliorated by using a sinusoidal amplitude grating that maximizes the diffraction in the +1 and -1 orders. These two beams can be used for interference, which will introduce light loss in the fluorescence channel only a factor of two larger than in the absence of the grating.

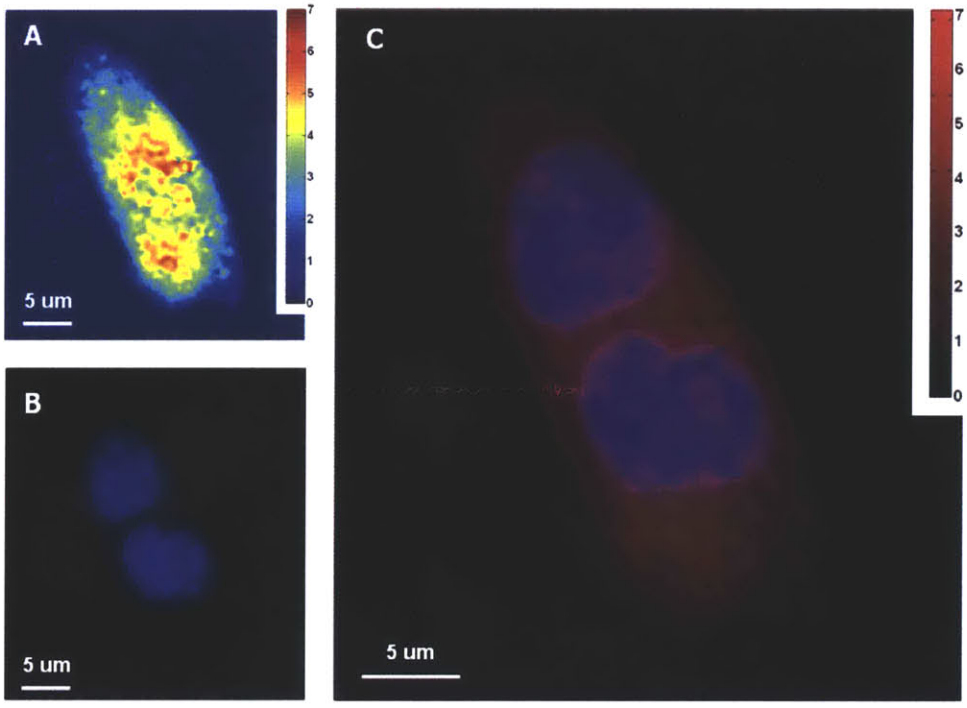

Figure 6. a) Quantitative phase image of a kidney cell. b) Fluorescence image of the DNA-stained cell. c) Overlaid images from a and b.

2.4 Capability of diffraction phase microscopy

DPM operates on the principle of laser interferometry in a common path geometry and provides full-field quantitative phase images of RBCs with 0.3 nm optical path-length stability

[20, 21]. Figure 7 shows the stability of DPM measured as follows. We collected signal on a background area of the sample which is free of cellular material. The full width half maximum (FWHM) displacement of this background gives ±0.3nm in terms of optical path length.

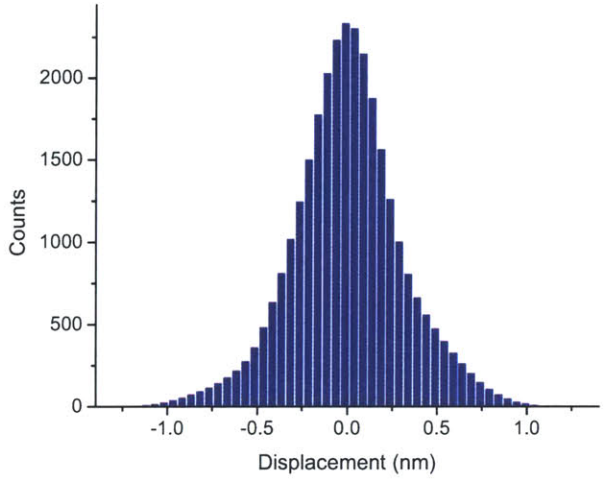

Figure 7. Histogram of displacement of background measured by DPM.

The instantaneous cell thickness map is obtained as $h(x,y,t)=(\lambda/2\pi\Delta n)\varphi(x,y,t)$, with λ=514 nm the wavelength of the laser light used, Δn=0.06 the refractive index contrast between the RBC and the surrounding PBS, and φ the quantitative phase image measured by DPM. For each RBC, images were acquired for 4 seconds at a rate of 128 frames per second. The optical path-length stability of 0.3 nm corresponds to a membrane displacement of 3.3 nm, which is the lower limit of our measurable range without using spatial or temporal averaging. Fig. 8 shows the static image of a RBC with DPM. This technique requires only a single of interferogram to reconstruct this three dimensional morphological map, thus the speed of this technique is limited only by the frame rate of the CCD.

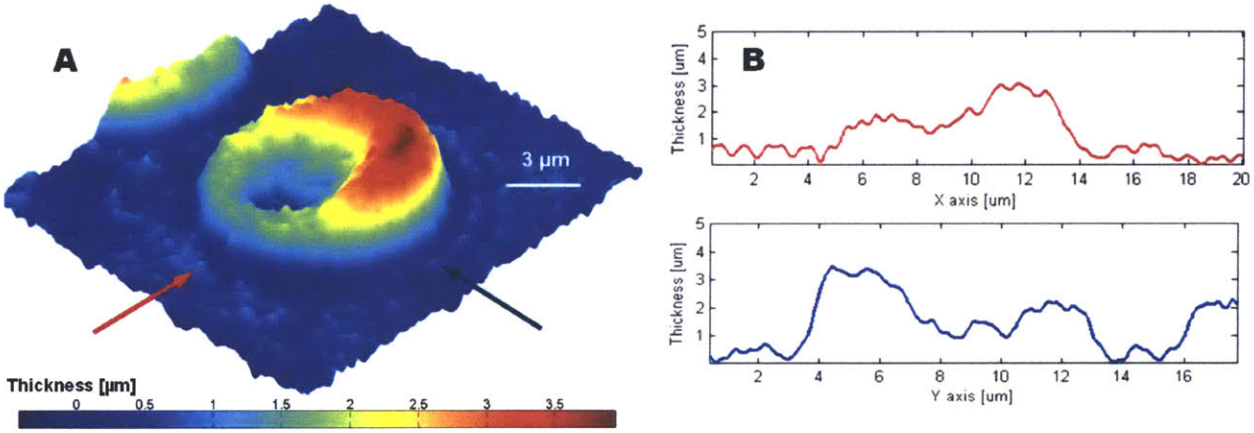

Figure 8. The static image of RBC measured with DPM; A. Topography map of RBC; B. cross section plots along arrows depicted in Fig. 7A

Chapter 3. RBC Membrane dynamics

3.1. RBC Membrane structure

Cell membranes are essential to the life of a cell. The plasma membrane defines the cell boundary and serves as the cell interface from the extra cellular environment [31]. Red blood cell membranes are dynamic, fluid structures. The lipid bilayer is a continuous double-layer arrangement of phosphor-lipid molecules, which provides the basic structure of the membrane and serves as a relatively impermeable barrier to the passage of water-soluble molecules. There are important protein molecules embedded in the lipid bilayer that determines the elastic properties of the membrane. Spectrin is a 100-nm-long, peripheral membrane protein that is the major component of the cytoskeleton that underlies the RBC membrane accounting for its biconcave shape and its flexibility. The tail ends of spectrin tetramers are linked together to short actin filaments and other cytoskeletal proteins, integrin in a junctional complex. Spectin network thus provides elasticity to the lipid bilayer of RBC.

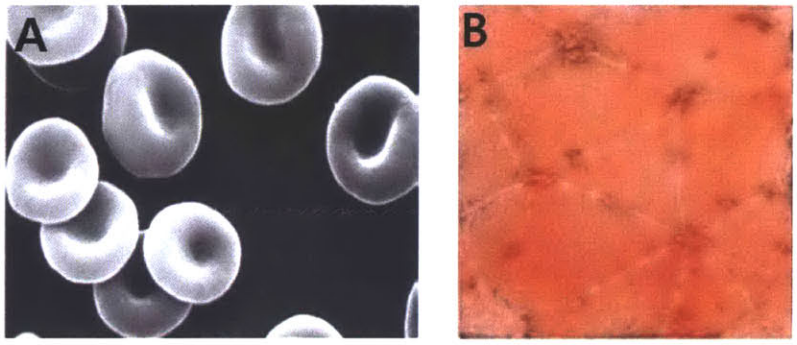

Figure 9. Scanning Electron Microscopy image of A. Red Blood Cell [29] B. membrane proteins [30]

Red blood cells must withstand large deformations during multiple passages through microvasculature and spleen sinusoids. This essential ability is diminished with senescence and disease. Cells affected by diseases such as spherocytosis, malaria, and sickle cell anemia depart from their normal discoid shape and lose their deformability [11]. Therefore, quantifying the mechanical properties of live RBCs provides insight into a variety of problems regarding the interplay of cell structure, dynamics, and function.

3.2. Dynamic complex modulus

The instantaneous cell displacement, $\Delta h(x, y, t)$ map was obtained by subtracting the time-averaged cell shape from each thickness map in the series. The mean squared displacement (MSD) map computed from Δh was Fourier transformed both in time and space to obtain the frequency domain representation of MSD, $\Delta h(q, \omega)^2$, where q is the modulus of the spatial wave

vector. The dissipative component (imaginary part) of the membrane response function is inferred from the fluctuation-dissipation theorem [27],

$$\chi''(q,\omega) = \frac{\pi\omega}{k_B T}\Delta h(q,\omega)^2 \tag{11}$$

where T is the absolute temperature and k_B is Boltzmann's constant. The storage component (real part) of the response function is obtained using the Kramers-Kronig relationship, which connects the real and imaginary parts of χ and reflects the causality of the system. We use the generalized Stokes-Einstein relationship (GSER) to retrieve the complex viscoelastic modulus

$$G(q,\omega) = \frac{1}{6\pi\Lambda}\frac{1}{\chi(q,\omega)} \tag{12}$$

where $\Lambda=2\pi/q$ is the spatial wavelength of the membrane fluctuations. The unit of $G(q, \omega)$ is Pa/m^2. The storage (elastic) modulus is the real part of G and the loss (viscous) modulus is the imaginary part of G. The spatially averaged complex modulus $G(\omega)$ is obtained by applying the FD theorem to $\Delta h^2(\omega) = 2\pi\int\Delta h^2(q,\omega)qdq$ and following the same procedure. The unit of $G(\omega)$ is Pa, which is commonly used in rheology.

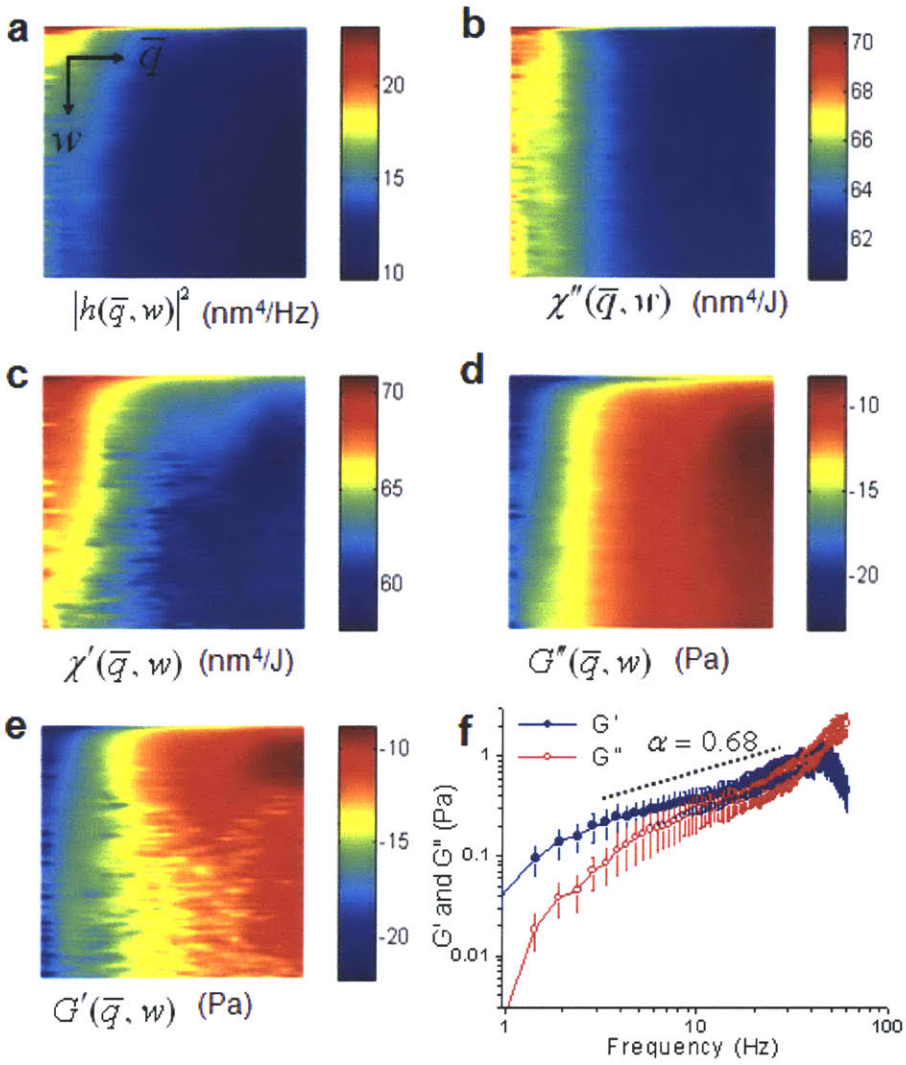

Figure 10. The procedures to retrieve complex modulus.

A typical measured nanoscale fluctuation power spectrum in both temporal frequency and spatial frequency domain, $|\Delta h(q,\omega)|^2$, is shown in Fig. 10a. The dissipative component (imaginary part) of the membrane response function is inferred from the fluctuation-dissipation theorem as in Eq. 11. (Fig. 10b). The storage component (real part) of the response function is obtained using the Kramers-Kronig relationship, which connects the real and imaginary parts of χ and reflects the causality of the system (Fig. 10c). I used the GSER to retrieve the complex viscoelastic modulus as in Eq. 12. Note that the unit of G(q, ω) is Pa/m^2. The loss (viscous) modulus G'' is obtained as the imaginary part of G (Fig.10d), and the storage (elastic) modulus G' is the real part of G (Fig. 10e). The spatially averaged complex modulus G(ω) is obtained by applying the FD theorem as

$$G(\omega) = \frac{1}{6\pi} \frac{1}{\int 2\pi q \Lambda \chi(q,\omega) dq}. \qquad (15)$$

The unit of G(ω) is Pa, which is commonly used in rheology.

The Fig.10A shows the correlation of RBC membrane fluctuation. The existence of such large correlations both in time and space is unexpected. Nevertheless, these coherence properties can be easily interpreted as the result of the viscoelastic properties of the cell membrane. Thus, assuming the model of a continuous elastic sheet under the action of both surface tension and bending, the membrane equation of motion can be written as[6]

$$\bar{h}(q,t)+\omega(q)h(q,t)=\Lambda(q)f(q,t), \tag{13}$$

where h is the height of the element of membrane, $\mathbf{q}$ the spatial wave vector, $\omega(q)=\left(\kappa q^3+\sigma q\right)/4\eta$, κ the bending modulus, σ the tension modulus, η the viscosity of the surrounding medium, f is the random force, and $\Lambda(q)=1/(4\eta q)$ is the Oseen tensor. It can be shown that the solution for displacement autocorrelation function can be expressed in the general form as [27]

$$\left\langle h(q,t)h(q,t+\tau)\right\rangle=\frac{\Lambda^2(q)}{\omega(q)}e^{-\omega(q)t}\otimes\left\langle f(q,t)f(q,t+\tau)\right\rangle, \tag{14}$$

where $\otimes$ denotes the temporal convolution operation and the angular brackets indicate temporal averaging. At thermal equilibrium, $\left\langle f(q,t)f(q,t+\tau)\right\rangle=2k_BT\delta(\tau)/\Lambda(q)$, which denotes the lack of temporal correlation in the force fluctuations. However, the elasticity of the membrane provides the motions with "memory", which results in a coherence time of the order of $1/\omega(q)$. Therefore, under the conditions of thermodynamic equilibrium, by exploiting the fluctuation-dissipation theorem (FDT) and GSER, the storage and loss moduli can be extracted from the fluctuation measurement. This approach has been used in the past for passive microrheology probed by embedded colloids [26,27].

To what extent active proteins contribute to the amplitude of the nanoscale motions of RBC membranes is still essentially an open question. Previous experiments on ATP-depleted cells seem to suggest that metabolic motions are significant [27]. Recent theoretical work predicted that such deterministic component should reflect itself in non-Gaussian distributions of measurement displacements [15].

3.3 Optical Microrheology of RBC

Blood samples were collected in vacutainer tubes containing Ethylene diaminetetra acetic acid to prevent blood coagulation. The whole blood was centrifuged at 2000 g at 5oC for 10 minutes to separate the RBCs from the plasma. The RBCs were then washed three times. The cells were resuspended in an isotonic solution of PBS at a concentration of 10% by volume. Droplets of the suspension were sandwiched between two cover slips and imaged at room temperature. A total of 90 cells were imaged over a period of 4 seconds, at a rate of 128 images per second: DC (N=30), EC (N=30), SC (N=30). Our samples were composed of normal, untreated RBCs. However, cells with abnormal morphology formed spontaneously in the suspension (ECs and SCs). RBCs were separated into three groups corresponding to their shapes: discocytes, echinocytes, and spherocytes. In rare occasions, some cells are not sitting flat on the glass substrate, which is apparent from the profile of the phase image. In order to avoid complications, we simply remove these cells from the batch. The shape effects, i.e. tangential

components of the fluctuations, are currently neglected in our analysis, which is justified because they affect significantly only the low-q region of our measurements.

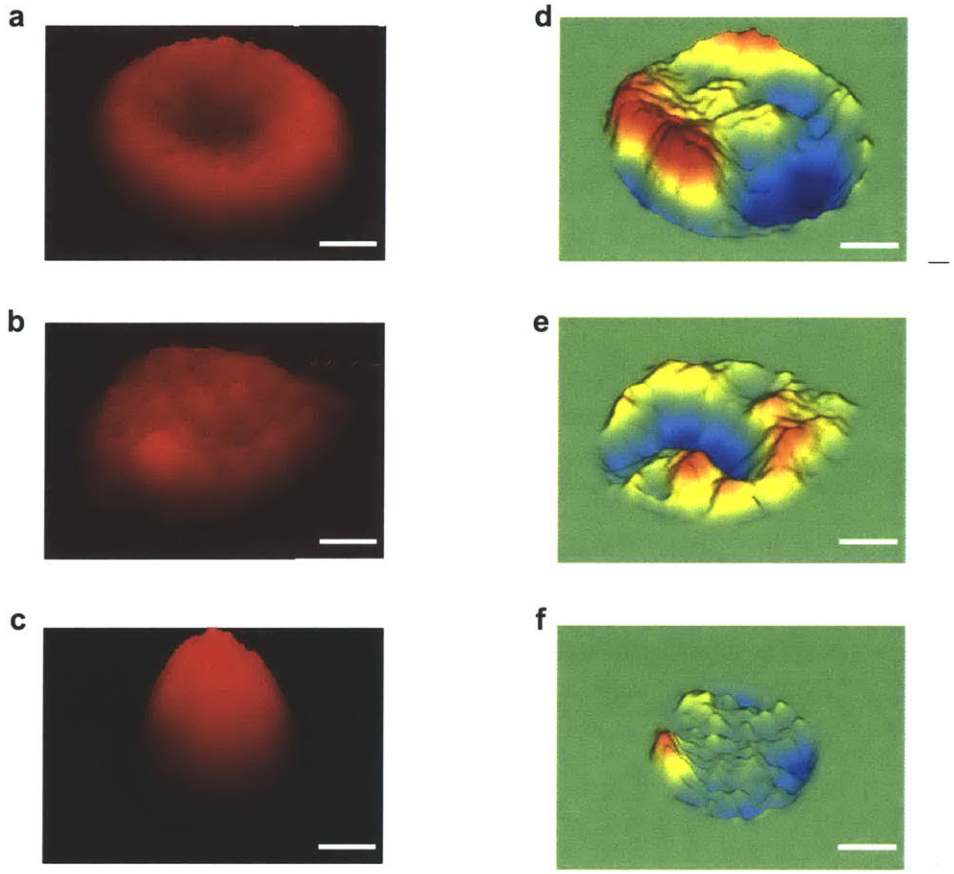

Figure 11. a-c) RBC profiles. d-f) Instant displacement maps (colorbar in nm and scale bar is 1.5μm).

It is well known that the RBC cytoskeleton consists of a two-dimensional protein (spectrin) network, which is tethered to the fluidlike bilayer and provides the necessary shear resistance [22]. However, little is known about the molecular and structural transformations that take place in the membrane as it loses its elasticity during shape change. In order to characterize the time-averaged (static) behavior of the membrane elasticity, We mapped the cells in terms of an equivalent spring constant k_e, by assuming elastic storage of thermal energy, $k_B T/2 = k_e \left\langle \Delta h^2 \right\rangle / 2$ (Fig. 12). This spatially-resolved representation reveals material inhomogeneities especially in ECs and SCs. Remarkably, the center ("dimple") region of normal cells (DCs) appears stiffer than the rest of the cell, which is likely due to a combination of the geometrical (i.e. high curvature) and structural properties of that membrane area [18]. The highly inhomogeneous k_e map associated with ECs

may indicate topological defects in the cytoskeleton mesh. On average, SCs are characterized by an elastic constant which is 4 times higher than that of DCs. The average elastic constant value for DCs lower than what was measured by micropipette aspiration [23] and electric field deformation [13]. However, this apparent discrepancy can be easily explained by noting that these two techniques probe large cell deformations, while our technique measures much smaller membrane displacements in the absence of external stress, i.e. explores the *linear* viscoelastic regime.

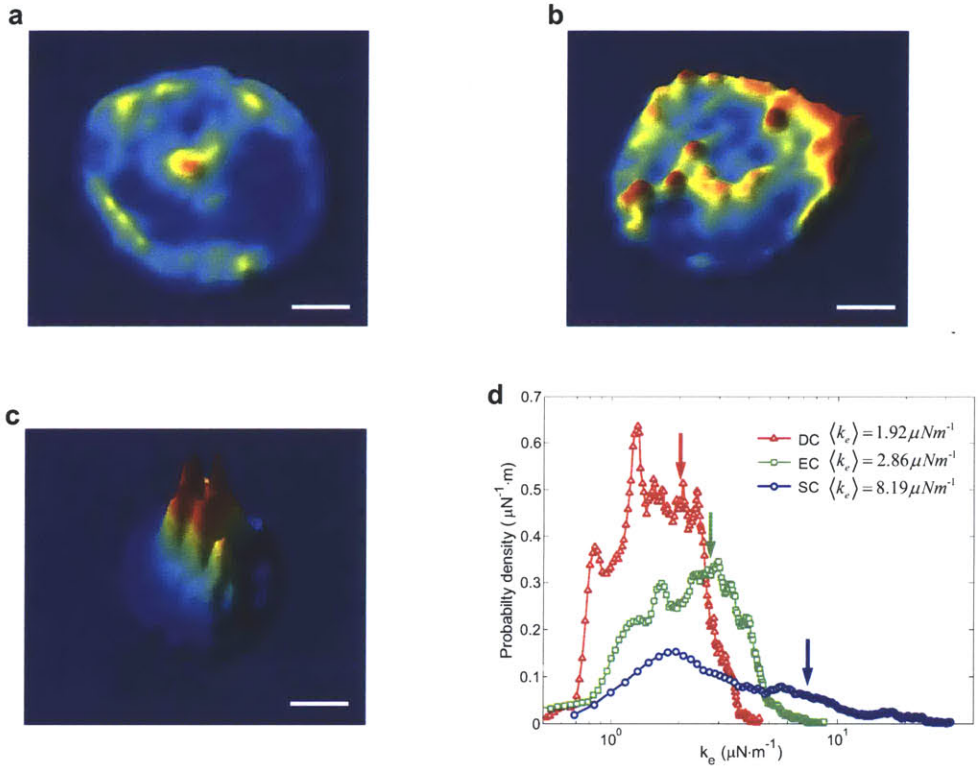

Figure 12. Maps of the apparent spring constant for DC (a), EC (b), and SC (c). Colorbars indicate μN/m and scale bar is 1.5μm. d) The corresponding histograms of spring constants, with the arrows indicating the mean values, $<k_e>$.

In order to extract the frequency-dependent storage and dissipation moduli associated with the RBC membrane, we employed the fluctuation-dissipation (FD) theorem and the generalized Stokes-Einstein relationship, as described in the section 3.2. This approach has been used in the past for passive microrheology probed by embedded colloids [24]. The viscoelastic moduli measured with our technique depend on both the spatial and temporal frequency, $G(q,\omega)$.

Figure 13 shows the viscoelastic moduli associated with the 3 morphology groups at 2 different spatial wavelengths. We found a consistent trend of increasing storage and loss moduli during the DC-EC-SC transition for all the frequencies, which reflects the gradual cell stiffening. Notably, at the spatial wavelength Λ=1 μm, G' and G'' for ECs and SCs overlap almost completely over the entire frequency range. This implies that at such small spatial scales a very slight change in shape, from DC to EC, produces a dramatic effect on viscoelasticity. By contrast,

the behavior at Λ=4 μm indicates that G' and G'' for SC are consistently higher than for ECs. Thus, the change in viscoelasticity associated with the DC-EC-SC shape impairment onsets at the smallest spatial scales and progressively evolves towards larger wavelengths. Such behavior can be accounted for by assuming that the cytoskeleton mesh evolves from a perfect protein lattice, with intact connections to the bilayer, to a state characterized by larger and larger defects.

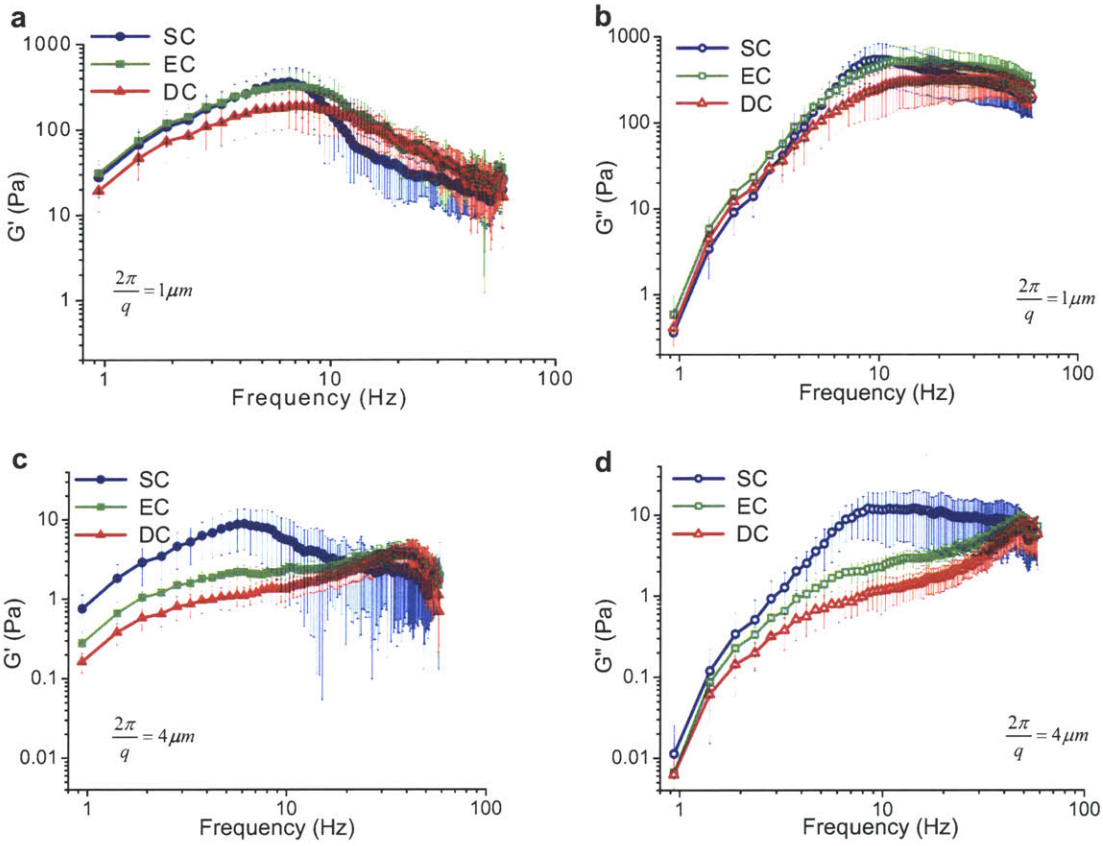

Figure 13. The viscous and elastic moduli for the three cell groups at two different spatial wavelengths Λ, as indicated. The error bars are the result of cell-to-cell variations, within each group, DC (N=30), EC (N=30), SC (N=30).

By spatially integrating the measured response function $\chi(q,\omega)$, we obtaine the overall dynamic behavior of G' and G'' (Fig. 14). For all the cell shapes, there is a transition frequency for which the elastic behavior becomes dominant. From the loss tangent representation (fig. 14d), it can be seen that, in the case of ECs, this transition occurs at a much lower frequency. The G' frequency dependence becomes gradually weaker, which implies that the DC-EC-SC morphological path is accompanied by a liquid-glass transition in terms of membrane viscoelasticity.

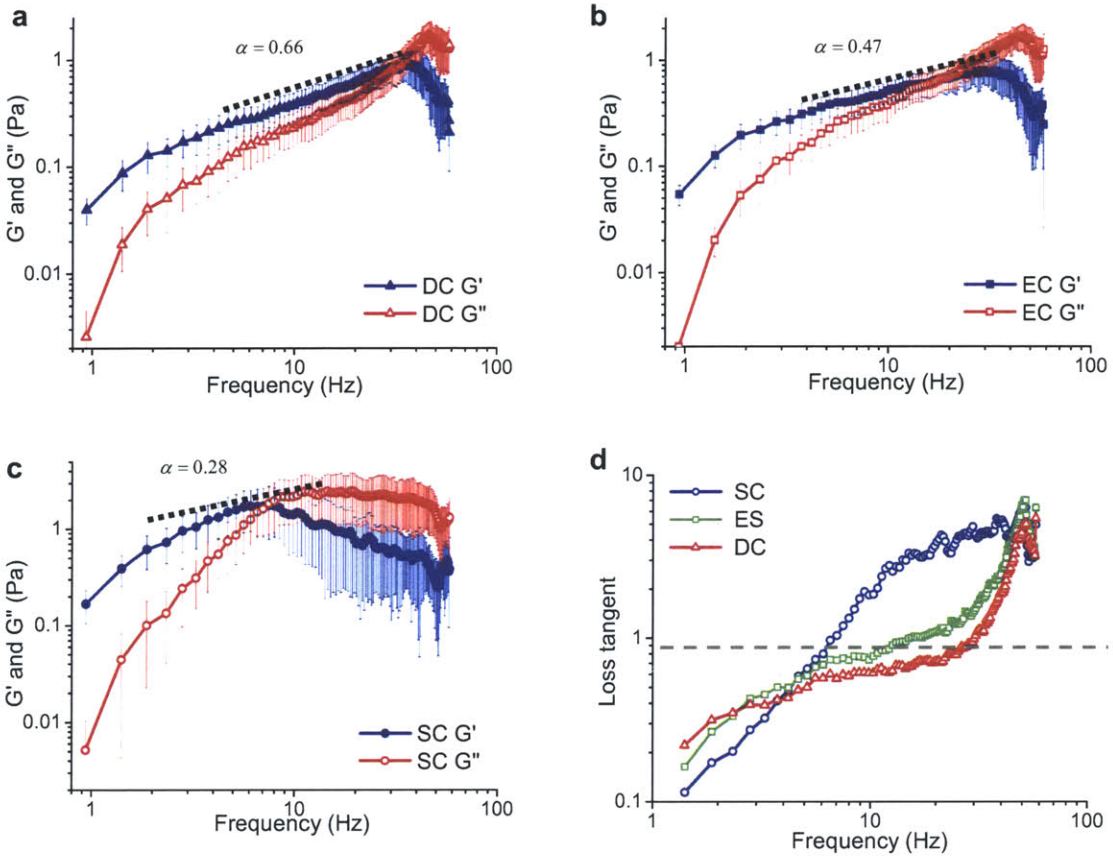

Figure 14. a-c) The spatially-integrated viscous and elastic moduli for the three groups, as indicated. The dotted lines indicate power law dependence of exponent α. d) The loss tangent for each group, as indicated.

Chapter 5. Conclusion and future directions

This thesis has presented a novel methodology for extracting the full visco-elastic information of live cell membranes. We developed both a quantitative phase imaging instrument based on optical interferometry and a theoretical framework for data analysis and interpretation relying on the fluctuation-dissipation theorem. The full complex modulus ($G=G'+iG''$) of the red blood cells in terms of both temporal (w) and spatial frequency (q) behavior was retrieved in a non-contact measurement scheme for the first time, to our knowledge. The experiments were performed with the diffraction phase and fluorescence microscope developed for the research, which provides the topological RBC information with nanometer accuracy at the millisecond scale.

This information is used to retrieve the dynamic and spatial behavior of red blood cell membranes during the process of morphological deterioration, i.e. during the discocyte-echinocyte-spherocyte shape transition. We found that the dynamics of the cell membrane correlates strongly with cell morphology. Thus, the results show that the cell evolution from a normal, discoid shape to a spheroid can be interpreted from a viscoelastic point of view as a liquid-solid transition. We anticipate that this non-contact procedure of quantifying cell membrane rheology will have important applications to understanding the membrane biophysics in various biochemical conditions. This description of the RBC shape-dynamics relationship can provide a detailed framework for understanding of RBC mechanical properties in health and disease. In addition to its clinical relevance, understanding dynamic properties of RBCs is of interest to membrane biology and basic studies of cellular dynamics. Mature RBCs lack nuclei and other major organelles and are uniformly filled with hemoglobin. As a result, RBCs are a highly sought model for studying cell membrane dynamics with broad implications in science and technology [33,34].

References

1. E. Ruestow, *"A look back: The Microscope"*, Am J Gastroenterol 10, 3046 (1999)
2. F. Zernike, *"How I discovered phase contrast"*, Science, *121*, 345-349 (1955).
3. J Goldstein, *Scanning Electron Microscopy and X-Ray Microanalysis*, New York : Kluwer Academic/Plenum Publishers, (2003)
4. G. Binnig et al, *"Atomic Force Microscope"*, Phys Rev Letts, 56, 930, 1986
5. G. Popescu et al, *"Fourier phase microscopy for investigation of biological structures and dynamics"*, Opt. Lett., 29, 2503-2505 (2004).
6. T. Ikeda et al, *"Hilbert phase microscopy for investigating fast dynamics in transparent systems"*, Opt. Lett. , 30, 1165-1168 (2005).
7. G. Popescu et al, *"Diffraction phase microscopy for quantifying cell structure and dynamics"*, Opt Lett, 31, 775-777 (2006).
8. P Marquet et al, *"Digital holographic microscopy: a noninvasive contrast imaging technique allowing quantitative visualization of living cells with subwavelength axial accuracy"*, Opt Lett, 30, 468-470 (2005)
9. C. Fang-Yen et al, *"Imaging voltage-dependent cell motions with heterodyne Mach-Zehnder phase microscopy"*, Opt Lett, (in press)
10. A1. D. Hognboom et al, *"Three-dimensional images generated by quadrature interferometry"*, Opt. Lett. 23, 783 (1998)
11. S. Suresh, *"Mechanical response of human red blood cells in health and disease: Some structure-property-function relationships"*, Journal of Materials Research, 21, 1871-1877 (2006).
12. G. Bao and S. Suresh, *"Cell and molecular mechanics of biological materials"*, Nature Mat. , 2, 715-725 (2003).
13. D. E. Discher et al., *"Molecular maps of red cell deformation: hidden elasticity and in situ connectivity"*, Science, 266, 1032-5 (1994).
14. H. Engelhardt et al., *"Viscoelastic properties of erythrocyte membranes in high-frequency electric fields"*, Nature, 307, 378-80 (1984).
15. M. Dao et al., *"Mechanics of the human red blood cell deformed by optical tweezers"*, Journal of the Mechanics and Physics of Solids, 51, 2259-2280 (2003).
16. M. Puig-de-Morales et al., *"Viscoelasticity of the humar red blood cell"*, J. Appl. Physiol., under review.
17. A. Zilker et al., *"Spectral-Analysis Of Erythrocyte Flickering In The 0.3-4-Mu-M-1 Regime By Microinterferometry Combined With Fast Image-Processing"*, Phys. Rev. A, 46, 7998-8002 (1992).
18. S. Tuvia et al., *"Cell membrane fluctuations are regulated by medium macroviscosity: Evidence for a metabolic driving force"*, Proc. Natl. Acad. Sci. U.S.A., 94, 5045-5049 (1997).
19. N. Gov et al., *"Cytoskeleton confinement and tension of red blood cell membranes"*, Phys. Rev. Lett., 90, 228101 (2003).
20. G. Popescu et al., *"Optical measurement of cell membrane tension"*, Phys. Rev. Lett., 97, 218101 (2006).
21. G. Popescu et al., *"Diffraction phase microscopy for quantifying cell structure and dynamics"*, Opt Lett, 31, 775-777 (2006).
22. Y. K. Park et al., *"Diffraction phase and fluorescence microscopy"*, Opt. Exp., 14, 8263 (2006).
23. J. B. Fournier et al., *"Fluctuation spectrum of fluid membranes coupled to an elastic meshwork: jump of the effective surface tension at the mesh size"*, Phys. Rev. Lett., 92, 018102 (2004).
24. R. Waugh et al., *"Thermoelasticity of red blood-cell membrane"*, Biophys. J., 26, 115-131 (1979).

25. T. G. Mason and D. A. Weitz, "*Optical measurements of frequency-dependent linear viscoelastic moduli of complex fluids*", Phys. Rev. Lett., 74, 1250-1253 (1995).
26. G. Popescu et al, *"Coherence properties of cell membrane dynamics"*, Phys. Rev. E., (under review)
27. Y. K. Park et al, *"Optical measurements of red blood cell rheology"*, Nature materials, (under review)
28. S. Tuvia et al., "*Cell membrane fluctuations are regulated by medium macroviscosity: Evidence for a metabolic driving force",* Proc. Natl. Acad. Sci. U. S. A., 94, 5045-5049 (1997).
29. http://web.ncifcrf.gov/rtp/ial/eml/rbc.asp
30. http://www.lbl.gov/Science-Articles/Archive/LSD-single-gene.html
31. TL Steck et al, "*The organization of proteins in the human red blood cell membrane: a review"*, Journal of Cell Biology, 62: 1-19 (1974)
32. G. Popescu et al, *"Optical measurement of cell membrane tension*", Phys. Rev. Lett., 97, 218101 (2006)
33. R. Lipowsky, *The conformation of membranes,* Nature, 349, 475-81 (1991).
34. E. Sackmann, *Supported membranes: Scientific and practical applications,* Science, 271, 43-48 (1996).